

Supplementary Data for

Seismic properties of the Nazca oceanic crust in southern Peruvian subduction system

YoungHee Kim¹

Robert W. Clayton²

¹ School of Earth and Environment Sciences, Seoul National University

² Seismological Laboratory, California Institute of Technology

This supplementary file describes (1) data processing for teleseismic receiver function (RF), (2) RF amplitude inversion, and (3) calculation of velocities of candidate phases from experimental mineral physics data.

1. Data processing for teleseismic receiver function

Identification of strong and sharp amplitudes of the P-to-S converted phase (hereafter, Ps) is crucial in this analysis. We try two different rotation coordinate systems (R-T-Z; e.g., Zhu and Kanamori, 2000) and (L-Q-T; e.g., Vinnik, 1977) to examine variations of the converted amplitudes. Phillips et al. (2012) and Phillips and Clayton (2014) used the R-T-Z coordinate system to identify the overall Peruvian crustal and slab structure using the same seismic network data. Yuan et al. (2000) and Sodoudi et al. (2011) used the L-Q-T coordinate system to image the slab structure beneath northern Chile. In this study, we only use subsets of the stations in the seismogenic zone (from the coast to the inland, up to 150 km; Fig. 2), which show clear Ps conversions at the top and bottom interface of the subducting crust. After the coordinate transformation, the R (or L) component seismograms are deconvolved with Z (or

Q) component seismograms at each station to obtain radial receiver functions (RFs). The RF calculation is done in the time domain, with Gaussian parameter of 4 and maximum 100 picks or iterations. The high frequency content (up to 1 Hz) in the prepared data and the iterative time domain deconvolution minimize waveform interference caused by the timing and amplitude variation due to slab dip and slowness (e.g., Song and Kim, 2012).

For the RF, the amplitude of the conversion is imaged (e.g., Supplementary Figs. S1 and S2), and the peak of the RF pulse indicates the discontinuity interface with its polarity controlled by the impedance contrast across the discontinuity. We notice the RF amplitudes appear stronger in L-Q-T coordinate system than in R-T-Z coordinate (Supplementary Fig. S1), and hence select the L-Q-T for measuring the amplitude of the converted phases. We then measure the amplitudes of the negative-positive pair in each RF, normalized by its maximum amplitude. Supplementary Fig. S2 shows example RFs computed at a single station in each seismic line, with the top plate interface locations highlighted by an arrow. Each station has a minimum of 20 traces. The collection of the RF amplitudes for all the selected stations is used in the inversion, which we describe in Section 4.2.

2. Receiver Function (RF) amplitude inversion

The inversion capability using the RF amplitudes was previously demonstrated based on the linearized Zoeppritz equation assuming small incidence angles, which was suitable for conversions along the horizontal Cocos plate segment (Kim et al., 2010). Using the same method, Kim et al. (2012) further used Bayesian sampling in the inversion for S wave velocities and density of the LVZ and LOC, to account for the uncertainty in the reference model for the volcanic arc. We briefly highlight the method in this section.

The method utilizes the RF amplitude information of the P - to - S converted phases in the four - layer model (continental crust (CC)/mantle lithosphere (ML), upper and lower oceanic crust (LVZ and LOC, respectively), and oceanic mantle (OM)) (Fig. 4). We obtain three different cases when the P wave is transmitted as a P or S wave at the top and bottom of the oceanic crust. The case 1 is when there is no conversion; the case 2 when the P wave is converted into S wave at the top of the LVZ; and the case 3 when the P wave is converted into S wave at the bottom of the LOC. By denoting the transmission coefficient at the interface as T for simplicity, we can express the transmission coefficient for each case (T^{CASE1} , T^{CASE2} , and T^{CASE3}) as shown in Fig 4. T_0 denotes the amplitude arriving at the bottom of the layer, and the subscript indicates the travel path of converted P or S wave at each interface, numbered as 3 (OM to LOC), 2 (LOC to LVZ), and 1 (LVZ to ML (or CC)). By dividing the transition coefficients for the case 2 and 3 by the case 1, we can obtain the transmission response at LVZ and LOC.

For the inversion, we use Zoeppritz equation for sub-critical plane-wave transmission coefficient between two elastic half-spaces (Aki and Richards, 2002):

$$T^{PS} = \frac{p\alpha}{2\cos j} \left[\left(1 - 2\beta^2 p^2 - 2\beta^2 \frac{\cos i \cos j}{\alpha} \frac{\Delta\rho}{\beta} \right) \frac{\Delta\rho}{\rho} - 4\beta^2 \left(p^2 + \frac{\cos i \cos j}{\alpha} \frac{\Delta\beta}{\beta} \right) \frac{\Delta\beta}{\beta} \right]$$

where p represents the ray parameter, α the P-wave velocity, β the S-wave velocity, ρ the density, and i and j the incident and transmitted angles, respectively. By considering the case with no conversions as a reference ray, the transmission coefficients T^{PS} at the top and bottom of the oceanic crust can be effectively isolated and used in the inversion. Assuming the small angle approximation (thus $p^2 \rightarrow 0$), the equation above is reduced as follows:

$$T^{PS} = \frac{p\alpha}{2} \left[\left(1 - \frac{2\beta}{\alpha} \right) \frac{\Delta\rho}{\rho} - \frac{4\beta}{\alpha} \frac{\Delta\beta}{\beta} \right]$$

We use least squares inversion to obtain shear wave velocities and densities. The data set for the inversion are the measured amplitude height of the negative and positive RF pulses normalized by the P wave pulse arriving at 0 s. In addition, the separation in time is used to invert for the thickness.

3. Velocities of candidate phases from experimental mineral physics data

Figure 7b (inset) shows the V_p/V_s as a function of V_s of candidate mineral phases such as amphibole, antigorite, lawsonite, zoisite, and pyroxene, and candidate rocks such as eclogite and gabbro, computed at different pressure (P)–temperature (T) conditions corresponding to depths of ~40-120 km for southern Peru. Seismic velocities for each candidate phase are computed using experimentally determined (see Supplementary Table S1 of Kim et al., (2012) for the values used in the analysis), and third-order finite strain theory (Duffy and Anderson, 1989). The gabbro is computed using the Voigt–Reuss–Hill (VRH) approximation on the combination of 50% plagioclase and 50% pyroxene (Mavko et al., 2003). The elastic properties of candidate phases are then computed by considering (1) without the presence of a fluid and (2) with needle-, sphere-, and penny-shaped, water-filled cracks with 10% porosity in each phase assemblage, calculated based on the Kuster and Toksöz formulation (Mavko et al., 2003; refer to Kim et al. (2012) for details). Each ellipse in Figure 7 includes the P – T ranges, different crack geometries, and uncertainties in the elasticity data. The major axis of each ellipse is primarily controlled by the P – T conditions with different depths and the minor axis by various crack geometries. The lower-right area of each ellipse corresponds to high P – T values whereas the upper-right area represents low P – T (Figure 7b, inset). Calculated velocities from the needle-shaped, water-filled cracks from 0% to 10% porosity

with different depths lie close to the area of the left part of the ellipse, and the velocities from the sphere-shaped lie close to the velocities from the needle-shaped, but characterized by higher V_s than those from the needle-shaped ones (Kim et al., 2012). On the other hand, the velocities from the penny-shaped ones lie close to the area of the right part of the ellipse (Kim et al., 2012). In addition, we also consider elastic anisotropy of antigorite and texture observations in a natural serpentinite (Bezacier et al., 2010).

References

Aki, K., Richards, P.G., 2002. Quantitative Seismology, 2nd ed. University Science Books, Sausalito, California.

Bezacier, L., Reynard, B., Bass, J.D., Sanchez-Valle, C., Van de Moortele, B., 2010. Elasticity of antigorite, seismic detection of serpentinites, and anisotropy in subduction zones. *Earth Planet. Sci. Lett.* 289, 198–208, <http://dx.doi.org/10.1016/j.epsl.2009.11.009>.

Duffy, T.S., Anderson, D.L., 1989. Seismic velocities in mantle minerals and the mineralogy of the upper mantle. *J. Geophys. Res.* 94 (B2), 1895–1912.

Kim, Y., Clayton, R.W., Jackson, J.M., 2010. Geometry and seismic properties of the subducting Cocos plate in central Mexico. *J. Geophys. Res.* 115 (B06310), doi:10.1029/2009JB006942.

Kim, Y., Clayton, R.W., Jackson, J.M., 2012. Distribution of hydrous minerals in the subduction system beneath Mexico. *Earth Planet. Sci. Lett.* 341–344, 58–67, doi:10.1016/j.epsl.2012.06.001.

Mavko, G., Mukerji, T., Dvorkin, J., 2003. *The Rock Physics Handbook: Tools for Seismic Analysis of Porous Media*. Cambridge University Press, Cambridge, UK.

Phillips, K. et al., 2012. Structure of the subduction system in southern Peru from seismic array data. *J. Geophys. Res.* 117, doi:10.1029/2012JB009540.

Phillips, K., Clayton, R.W., 2014. Structure of the subduction transition region from seismic array data in southern Peru. *Geophys. J. Int.* 196, 1889–1905, doi:10.1093/gji/ggt504.

Sodoudi, F., Yuan, X., Asch, G., Kind, R., 2011. High-resolution image of the geometry and thickness of the subducting Nazca lithosphere beneath northern Chile. *J. Geophys. Res.* 116, B04302, doi:10.1029/2010JB007829.

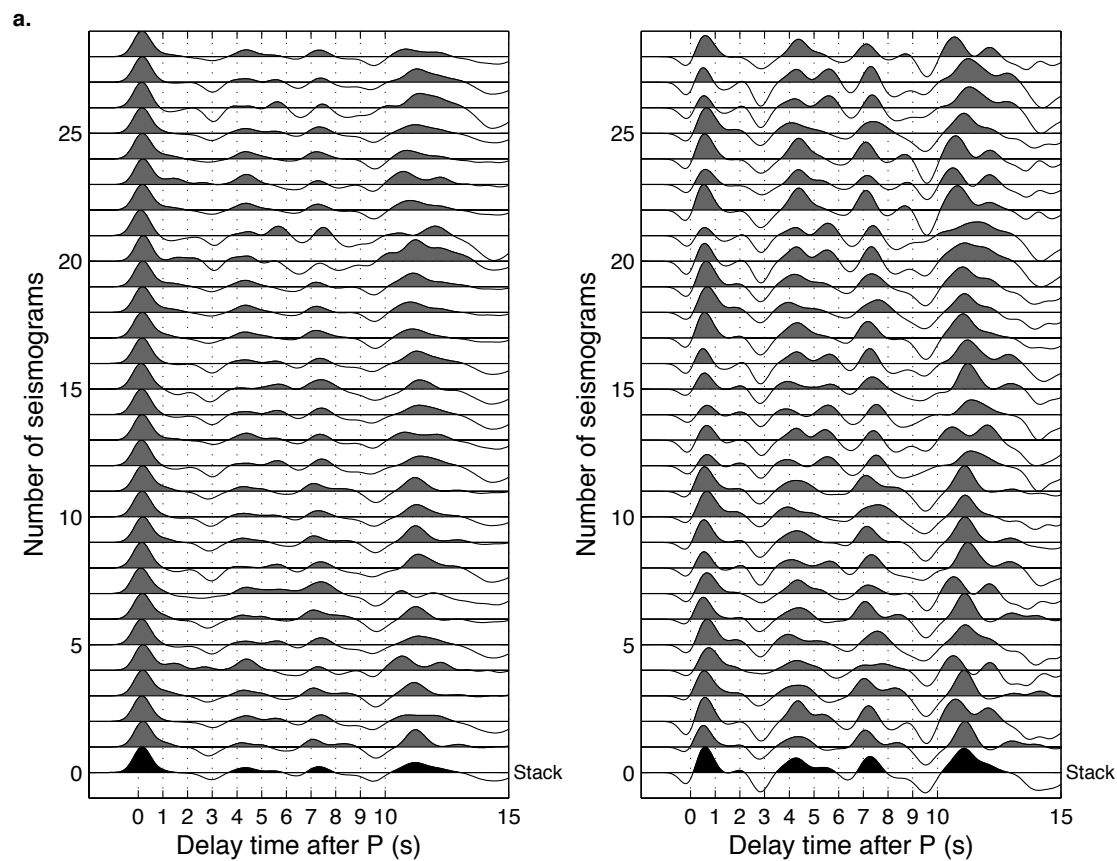
Song, T-R, Kim, Y., 2012, Localized Seismic Anisotropy associated with Slow Earthquakes beneath Southern Mexico. *Geophys. Res. Lett.* 39, L09308, doi:10.1029/2012GL051324.

Vinnik, L., 1977. Detection of waves converted from P to SV in the mantle. *Phys. Earth Planet. Inter.* 15, 39–45.

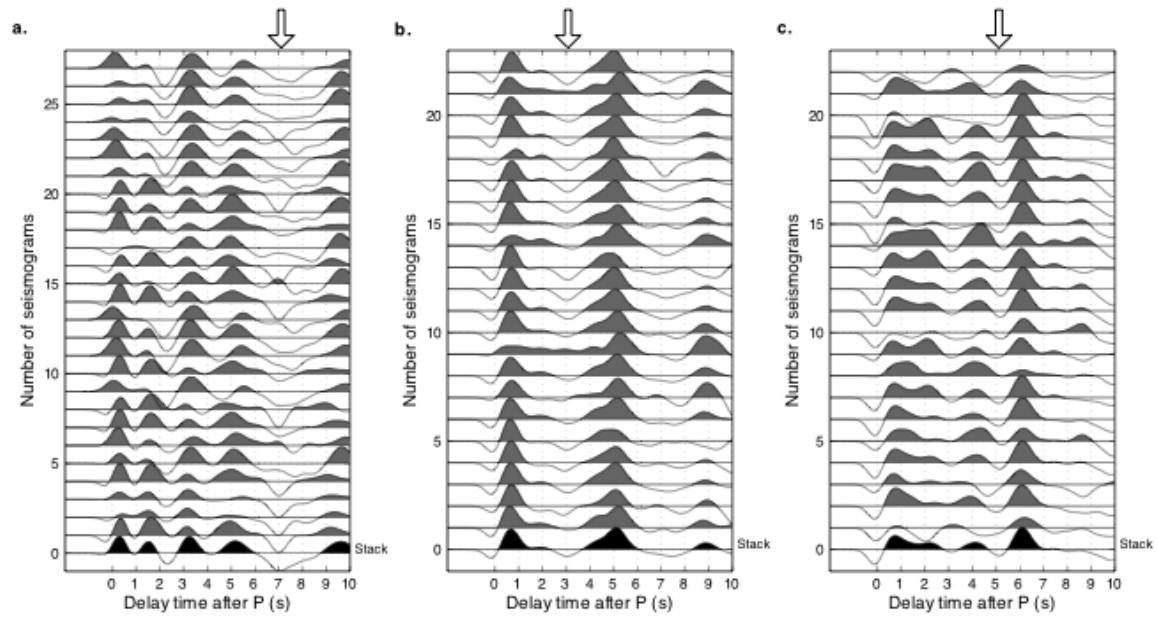
Yuan X., Sobolev, S.V., Kind, R., Oncken, O., Beck, G., Asch, G., Schurr, B., Graeber, F., Rudloff, A., Hanka, W., Wylegalla, K., Tibi, R., Haberland, Ch., Rietbrock, A., Glese, P.,

Wigger, P., Rower, P., Zandt, G., Beck, S., Wallace, T., Pardo, M., Comte, D., 2000. Subduction and collision processes in the central Andes constrained by converted seismic phases. *Nature*, 408, 958-961.

Zhu, L., Kanamori, H., 2000. Moho depth variation in southern California from teleseismic receiver functions. *J. Geophys. Res.* 105, 2969–2980.



Supplementary Fig. 1. Receiver functions (RFs) for station PG17 based on R-T-Z (a) and L-Q-T (b) coordinate systems. The station location is shown in Fig. 2. The RFs are aligned in the order of an increasing epicentral distance from second bottom to top. Stacked RFs for two coordinate systems are shown at the very bottom.



Supplementary Fig. 2. Receiver functions (RFs) based on the L-Q-T coordinate system for three stations (a. PE09; b. PG01; c. PH30). The locations for these three stations are shown in Fig. 2. The RFs are aligned in the order of an increasing epicentral distance from second bottom to top. Stacked RFs for two coordinate systems are shown at the very bottom. Top plate interface locations are highlighted by an arrow in each panel.

Supplementary Table 1. One-dimensional model for teleseismic migration.

Depth range (km)	V_p (km/s)	V_s (km/s)	Density (g/cm ³)
0 – 30	6.30	3.64	2.8
30 - 60	7.57	4.24	3.0
60 - 300	8.32	4.53	3.3

Supplementary Table 2. One-dimensional model for receiver function amplitude inversion.

V_p , V_s , and density in bracket are the range of values that we use for uncertainty estimates.

** denotes inverted.

Layer	V_p (km/s)	V_s (km/s)	Density (g/cm ³)
Continental crust	6.25 [6.0-6.5]	3.61 [3.46-3.75]	2.8 [2.69-2.85]
Mantle lithosphere	6.75 [6.5-7.0]	3.90 [3.75-4.04]	2.93 [2.85-3.01]
Low velocity zone	5.5 [5.0-6.0]	**	**
Lower oceanic crust	7.0 [6.7-7.3]	**	**
Oceanic mantle	8.25 [8.0-8.5]	4.76 [4.62-4.91]	3.41 [3.33-3.49]